Interaction between counter-propagating quantum Hall edge channels in the 3D topological insulator BiSbTeSe$_2$

Chuan Li,[1] Bob de Ronde,[1] Artem Nikitin,[2] Yingkai Huang,[2] Mark S. Golden,[2] Anne de Visser,[2] and Alexander Brinkman[1]

[1]*MESA+ Institute for Nanotechnology, University of Twente, 7500 AE Enschede, The Netherlands*

[2]*Van der Waals–Zeeman Institute, Institute of Physics, University of Amsterdam, 1098 XH Amsterdam, The Netherlands*

The quantum Hall effect is studied in the topological insulator BiSbTeSe$_2$. By employing top- and back-gate electric fields at high magnetic field, the Landau levels of the Dirac cones in the top and bottom topological surface states can be tuned independently. When one surface is tuned to the electron-doped side of the Dirac cone and the other surface to the hole-doped side, the quantum Hall edge channels are counter-propagating. The opposite edge mode direction, combined with the opposite helicities of top and bottom surfaces, allows for scattering between these counter-propagating edge modes. The total Hall conductance is expected to be integer valued only when the scattering is strong. For weaker interaction, a noninteger quantum Hall effect is expected and indications for this effect are measured.

I. INTRODUCTION

The quantum Hall effect (QHE) can be described by the formation of quantized edge state conduction. The conductance of quantum Hall edge modes in a semiconductor is given by $2nG_0$, where n is the number of modes (linked to the Landau level filling number of the bulk), the multiplication by two is to account for two spins, and $G_0 = \frac{e^2}{h}$ is the conductance quantum [1]. When the electronic dispersion of a material is given by the Dirac equation, the first bulk Landau level sits at the Dirac point and simply provides a conductance contribution of only $\frac{G_0}{2}$, as can be explained by the extra Berry phase of π that is obtained in a Landau orbit. For graphene, one then obtains an edge conduction of $4(n + \frac{1}{2})G_0$, where the factor of four comes from the twofold spin degeneracy and the twofold orbital degeneracy due to there being Dirac points at the crystallographic K and K' points [2].

After the discovery of topological insulators, it was soon understood that the Dirac cone of the topological surface state (TSS) of a three-dimensional topological insulator (TI) is not spin degenerate, except at particular Kramer's momenta. Like for graphene, the Berry phase argument provides an offset of $\frac{1}{2}$, and the direction of the conduction channels is determined by the position of the Fermi level in the Dirac cone with respect to the Dirac point (electrons versus holes). Every surface (e.g., top and bottom) then provides an edge conduction of $(n + \frac{1}{2})G_0$, rendering the TSS effectively equivalent to one-quarter of graphene [3]. The top (t) and bottom (b) surfaces of a 3D topological insulator posses Dirac cones of opposite helicities. When the two surfaces are gate tuned so that the Fermi energy in both systems is either above or below the Dirac point (i.e., two electron or two hole Fermi surfaces), the edge modes of the two surfaces propagate in the same direction, but with opposite helicity. Due to their orthogonality no scattering from one to the other is quantum mechanically allowed. In such a case, the parallel mode conductances add up, yielding an integer quantum Hall effect, i.e., the Hall conductance $G_{xy} = (n_t + n_b + 1)G_0$. This integer quantization has indeed been observed for 3D topological insulators such as BiSbTeSe$_2$ [4,5], (Bi$_{1-x}$Sb$_x$)$_2$Te$_3$ [6], HgTe [7], and magnetically doped topological insulators, where the role of the external magnetic field is replaced by an internal magnetization [8,9].

However, when the top and bottom surfaces of a 3D topological insulator are gate-tuned to different sides of the Dirac point (i.e., one electron and one hole Fermi surface) the edge modes of the two surfaces are counter-propagating, as shown in Fig. 1(a). In this case, the helicities of the states are equal as the sign reversal going from top to bottom surface is canceled by the sign reversal going from the electron to the hole side of the Dirac cone. This situation is different from the counter-propagating modes in a quantum spin Hall insulator (QSH) [10], where the mode conductance lacks the factor of $\frac{1}{2}$ and where counter-propagating modes at an edge have opposite spins and thus cannot scatter elastically into each other. See the Supplemental Material [11] for a comparison of the quantum Hall effect in different cases.

Here, we study the interaction between counter-propagating surface states in a three-dimensional topological insulator exploiting independent gate tuning of the upper and lower topological surface states of a BiSbTeSe$_2$ device. We observe noninteger quantum Hall conductance values likely due to the reduced scattering between the surface state modes by the use of a large separation between top and bottom surfaces. The noninteger (but rational) conductance values can be understood from the voltage probes being in perfect equilibrium with both the top and bottom edge modes. Modeling the conductance data enables extraction of a value for the probability of scattering between the top and bottom surface modes.

II. DEVICE FABRICATION AND LOW FIELD CHARACTERIZATION

As a three-dimensional topological insulator, stoichiometric BiSbTeSe$_2$ [4,13,14] is used because of its decent mobility and highly insulating bulk. For growth and details of the e-beam structuring, as well as realization of metal contacts and top and bottom gates, see the Supplemental Material [11]. Two devices have been characterized at low magnetic fields and both show similar behavior. One device was selected for the high-magnetic field measurements. Figure 1 depicts
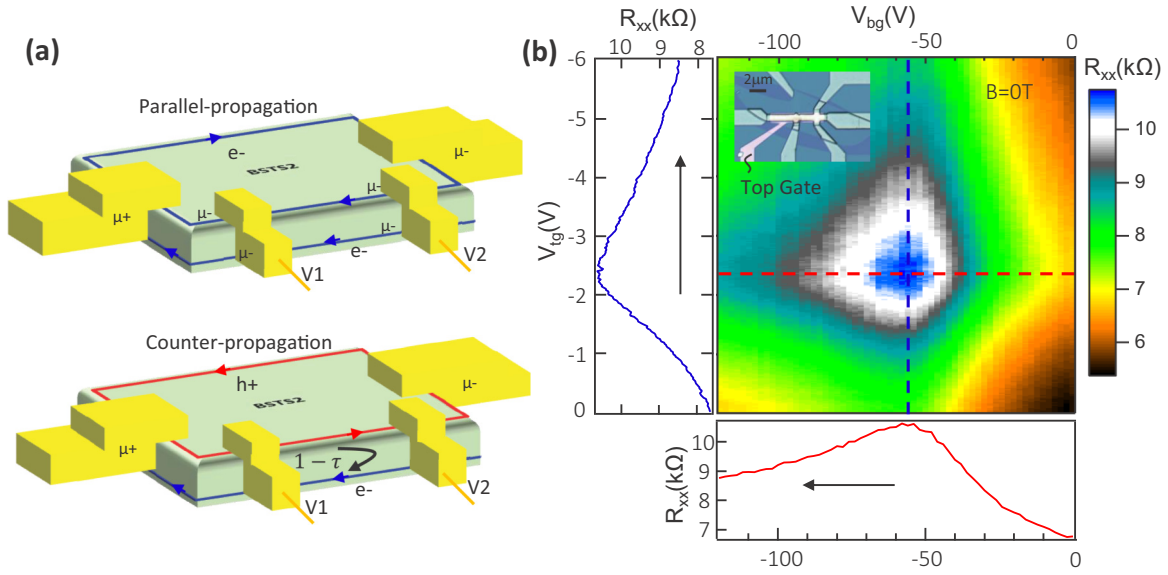
(a)

(b)

FIG. 1. (a) Schematic drawing of a dual-gated quantum Hall device with either parallel propagation or counter-propagation in the edge states of the topological bottom and top surfaces of a 3D topological insulator. In the case of parallel propagation (upper panel), the charge carriers move in the same direction and the edges of the surfaces form equipotential lines ($\mu_\pm$) [12]. For counter-propagation (lower panel), the electrons and holes come from different potential reservoirs (electrodes) and move in opposite directions. In this case, a nonzero probability exists for backscattering between the top and bottom surfaces, given by $(1 - \tau)$. (b) Two-dimensional gate map of the longitudinal resistance, R_{xx}, as a function of the top and back gate voltages at zero magnetic field. The maximum resistance indicates the chemical potential lying at the Dirac point. The color-coded line cuts showing R_{xx} versus gate voltages are also shown, as is an inset showing an optical microscopy image of the device, in which the top gate and the BiSbTeSe$_2$ flake are clearly visible. The black arrows indicate the sweep direction of the measurements.

the schematic layout of the experiment as well as an optical microscopy image of the device.

We measured the differential resistance for R_{xx} and R_{xy} at zero magnetic field in a Hall-bar-shaped sample while sweeping the top-gate and bottom-gate voltages independently. This gave the data presented in Fig. 1(b). A single maximum appears in the gate scan range of the map, at which the Fermi levels of both top and bottom surface states are tuned close to their respective Dirac points (DPs). Both top and bottom surfaces were found to be electron doped initially, meaning the DPs of both surfaces are positioned at negative gate voltage. To the left and below the 2D figure, the profiles of R_{xx} as a function of the top (back) gate voltage, V_{tg} (V_{bg}), are given for cuts indicated with a blue (red) line. The maximum of the profile as a function of the top-gate voltage does not depend on the back-gate voltage and vice versa, which means that the top and bottom gates only tune their proximate surface states. This shows that the two surfaces are decoupled, split as they are by the insulating bulk, consistent with both previous observations of decoupled BSTS surfaces [15] and with the significant thickness chosen for the flake (240 nm).

The independent gate tuning capability of the Dirac cones of the two topological surface states is also manifested in the Hall effect data at low magnetic field. Figure 2(a) shows the antisymmetrized R_{xy} Hall signal of top-gate sweeps recorded for different magnetic fields. With the bottom surface slightly electron doped ($V_{bg} = -40$ V), when the top gate crosses the DP, the slope of $R_{xy}(B)$ changes sign, which indicates that

we tune the top surface from being electron doped to hole doped. The figure at the bottom shows a sharp change from positive to negative value of R_{xy} as function of the top-gate voltage.

We deduced the carrier density from the R_{xy} data using a two-band model, in order to account for the top and bottom surface conduction contributions (from the independent gating of the two surfaces, the bulk contribution can be assumed to be negligible). In general, there are four fitting parameters (the top and bottom surface mobilities, μ_t and μ_b, and the two carrier densities, $\mathcal{N}_t$ and $\mathcal{N}_b$). However, in our case, we benefit from the results of high field measurements (shown and discussed in the Supplemental Material [11]) to estimate the gate dependence of the carrier density of both surfaces more accurately. This allows us to fix the carrier densities of two surfaces and use the two mobilities as the only fitting parameters. The results of the fitting, see Fig. 2(b), show that we can tune both the top and bottom surfaces to have very low carrier densities, and thus continuously tune the Fermi level through the DP. When the Fermi level is very close to the DP, rather than needing only two conductance channels, the fitting requires a third contribution. Most likely, this is not due to the side surfaces. In general, the etching steps in the Hall bar fabrication procedure result in a very poor mobility for the side surfaces. Moreover, the side surfaces are oriented parallel to the applied field, meaning that they do not contribute to the R_{xy} signal either. Most likely, the extra contribution arises from spatial charge fluctuations [16] in the 2D surface states, also observed for BiSbTeSe$_2$ [17]. From the multiband fit, the
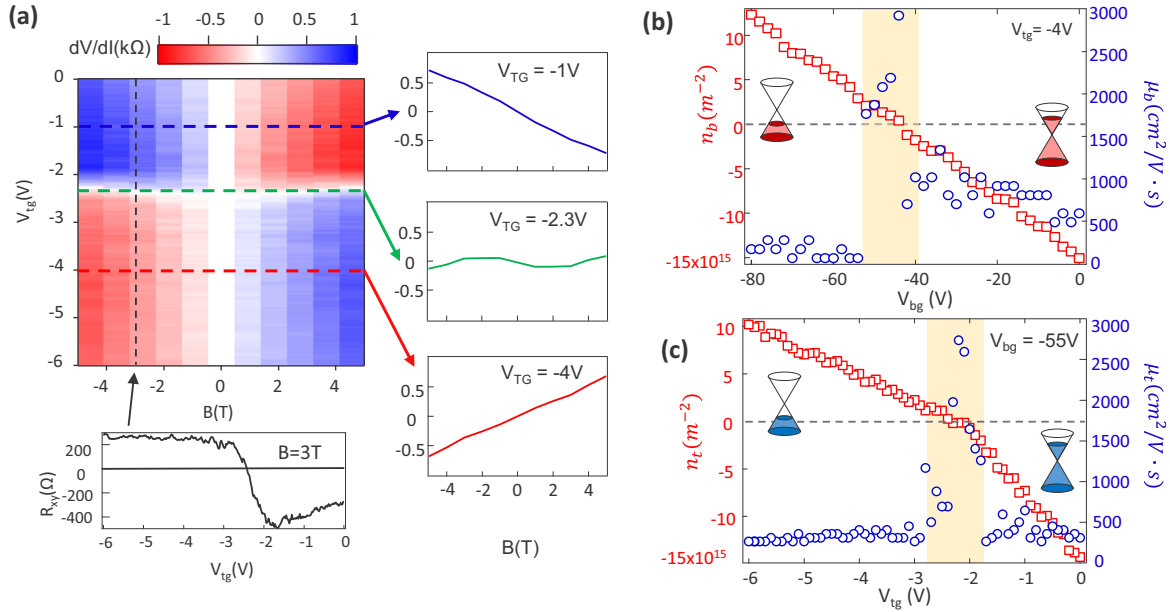
FIG. 2. (a) Antisymmetrized R_{xy} Hall data as a function of top-gate voltage and magnetic field for a fixed back-gate voltage ($V_{bg} = -40$ V). Hall resistance traces as a function of field for different top-gate voltages are shown to the right of the 2D map. The sign of the slope of R_{xy} versus B changes when the top surface is tuned from electron doped (blue) to hole doped (red). At the threshold top-gate voltage (green), the R_{xy} signal is almost flat due to a cancellation of the R_{xy}^t and R_{xy}^b signals. In the bottom figure, a plot of R_{xy} versus V_{tg} is plotted for a field of 2.3 T, and shows a sharp change when R_{xy} crosses zero. (b) Carrier density, $\mathcal{N}_b$, and mobility, μ_b, of the bottom surface as a function of back-gate voltage as the result of a multiband fit to the Hall data. The charge carrier density changes sign as the Fermi level is tuned through the Dirac point. Around the Dirac point (yellow shading), charge puddles give rise to a third conductance contribution. (c) Carrier density, $\mathcal{N}_t$, and mobility, μ_t, of the top surface as a function of top-gate voltage.

carrier density of these charge puddles is estimated to be about 5×10^{15} m^{-2}.

III. QUANTUM HALL MEASUREMENTS AND DISCUSSION

At high magnetic field, the Landau levels start to appear and form the conducting edge states. The two gates can be used to tune the Fermi level between different Landau levels (LLs). A gate map of unsymmetrized G_{xy} data at 15 T and -15 T and 50 mK is shown in Figs. 3(a) and 3(b). We can already see that the G_{xy} gate map is divided into several quasirectangular areas. These plateaus correspond to different filling factor combinations of $\nu_t = n_t + \frac{1}{2}$ and $\nu_b = n_b + \frac{1}{2}$. We indicate the different plateaus in brackets in a normalized G_{xy} map after (anti)symmetrizing the (R_{xy}) R_{xx} data (see Supplemental Material [11] for the details).

However, due to the moderate mobility (albeit state of the art for Bi based topological insulators) the Landau levels are not perfectly developed at a field of 15 T, and the formed edge states stay dissipative. As a consequence, we always observe nonzero (but strongly reduced) R_{xx} between two LLs, as well as a reduced G_{xy} value, which complicates the results and prevents a direct matching of experimental and theoretical results. For this, an additional analysis is applied (as will be explained further on).

To get a better understanding of the expected quantized Hall conductance in this combined system of two surface states, we modeled the system using the Landauer-Büttiker formula (see Supplemental Material [11] for the modeling

details). We theoretically expect an unusual noninteger Hall conductance in the regime for which the two surfaces are populated by charge carriers of opposite sign [lower panel of Fig. 1(a)], but equal helicity. Intuitively, when the coupling between electrons and holes is strong, the counter-propagating states counteract each other and will cancel when summing the Hall conductances, but this picture only holds when the counter-propagating filling factors are exactly opposite (e.g., $\nu_t = -\nu_b = \frac{1}{2}$). In general, counter-propagating edge modes start off from different current injection electrodes, and have, therefore, different chemical potentials; see also Fig. 1(a). If there is no interaction possible between the surface channels through the bulk, the only way to get equilibrium is to equalize the potential inside the metal electrodes. Using this as a boundary condition, we theoretically expect noninteger values for the Hall conductances in the counter-propagating regime, even for perfect transmission of the edge channels. The calculated and measured values are shown in Fig. 3(f). Cross-sectional cuts of the data are shown in Figs. 3(d) and 3(e).

Due to the imperfect edge channels at these moderate magnetic fields (i.e., $\mu B \ll 1$ not being fulfilled), the values for the Hall conductance deviate from the expected values, and R_{xx} does not go completely to zero. This effect becomes most apparent for the top-gate dependence of G_{xy} at constant bottom surface Landau level, as shown in Fig. 3(e), and is strongest in the regimes for which the surfaces are populated by charge carriers of opposite sign (we note that the mobility of the holes is generally lower than the mobility of the electrons in topological insulators, consistent with our observation in Fig. 2). Indeed, impurities or defects on the side surfaces of a
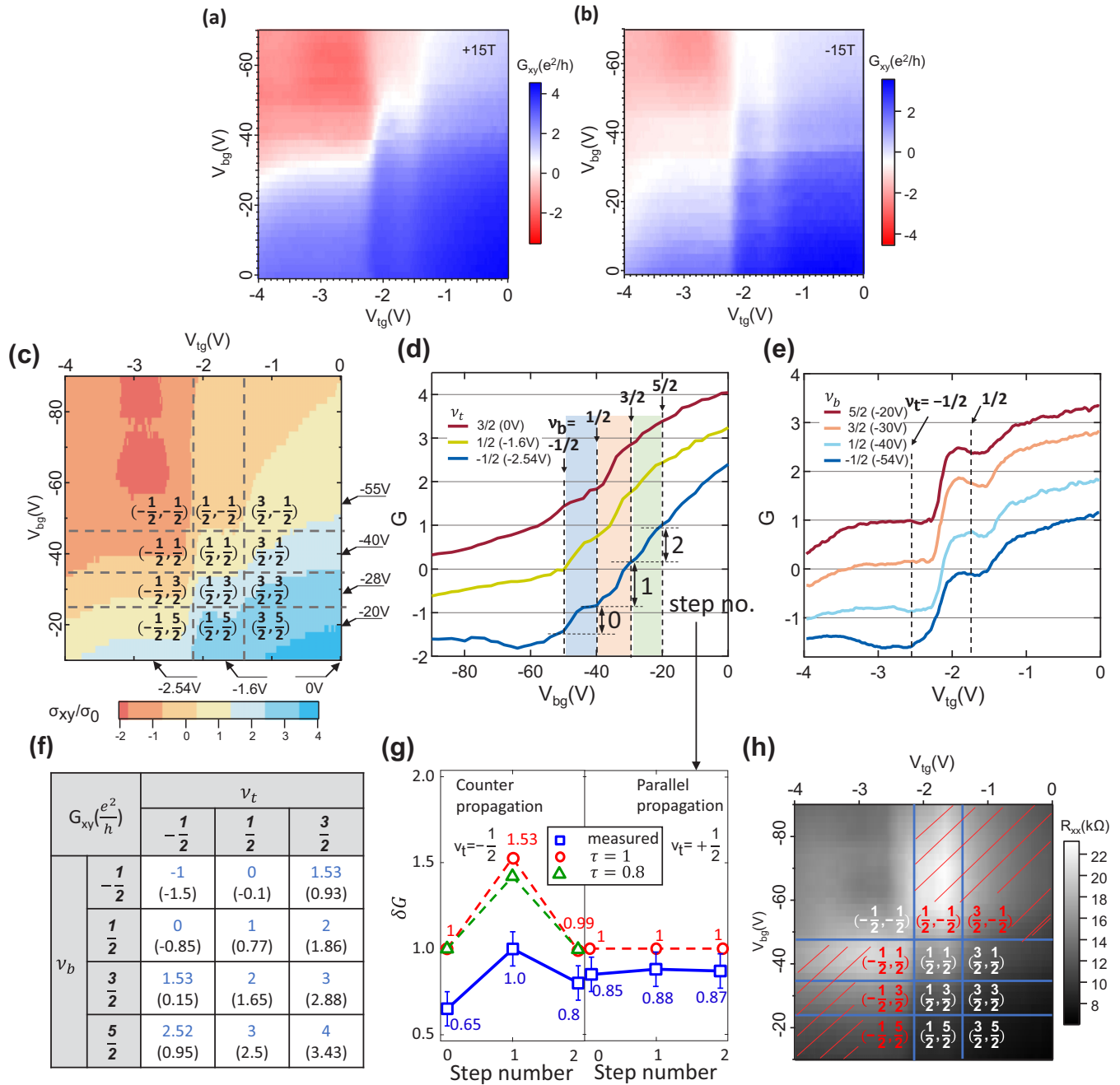
FIG. 3. (a),(b) Unsymmetrized Hall conductance G_{xy} as a function of top-gate voltage (V_{tg}) and back-gate voltage (V_{bg}) at $+15$ and -15 T. (c) G_{xy} gate map after (anti)symmetrization analysis. The dashed lines indicate the borders between plateaus corresponding to different filling factors, noted as (ν_t, ν_b). The voltage indicators on the outside of the frame mark the positions of the cross sections in the subsequent panels. (d) Back-gate voltage dependence of G_{xy} at the three values of ν_t shown in (f). The vertical, dashed lines indicate different ν_b. (e) Top-gate voltage dependence of G_{xy} at the four different ν_b's given in (f). The vertical, dashed lines now indicate different ν_t. (f) Expected values of the Hall conductance for different filling factors in units of $\frac{e^2}{h}$. The measured values are shown between brackets. (g) Measured and calculated values for the change in G_{xy} for successive bottom surface Landau levels, as indicated by the steps in (d) when going from one ν_b value to the next. Error bars are extracted from the averaging carried out of the gating map data. Left: $\nu_t = -\frac{1}{2}$ (counter-propagating modes). Right: $\nu_t = \frac{1}{2}$ (parallel propagation). The calculated step sizes are shown both for perfect transmission ($\tau = 1$) and for $\tau = 0.8$. (h) Longitudinal resistance, R_{xx}, at $B = 15$ T versus V_{tg} and V_{bg}. Blue solid lines indicate the borders of the Landau level plateaus. The hatched areas indicate regions with counter-propagating modes.

topological insulator are predicted to lead to hybridization of the edge states of the two surfaces [18].

However, the bottom surface shows better quantization values (perhaps due to better protection during device pro-

cessing); hence we use Fig. 3(d) rather than 3(e) for the subsequent analysis. Especially when we look at the change in the Hall conductance at constant ν_t when going from one ν_b to the other, a quantitative analysis can be made as regards

the nature of the coupling between counter-propagating edge modes. We plot both the calculated (red, green) and the measured (blue) Hall conductance changes (δG_{xy}) when changing ν_b in Fig. 3(g). The procedure to obtain the averaged experimental numbers from the full gating map is explained in the Supplemental Material [11]. The step numbers 0, 1, and 2 correspond, respectively, to $\nu_b = -\frac{1}{2} \rightarrow \frac{1}{2}$, $\frac{1}{2} \rightarrow \frac{3}{2}$, and $\frac{3}{2} \rightarrow \frac{5}{2}$. Note that all experimental values are lower than theoretically expected, likely due to the nonvanishing shunting conductance of the bulk states. Despite the overall lowering factor, for counter-propagating modes a clearly nonmonotonic change in the Hall conductance is experimentally observed around step 1 for $\nu_t = -\frac{1}{2}$, as predicted by the model. On the other hand, the Hall conductance change stays almost constant for parallel propagation, when $\nu_t = \frac{1}{2}$, also in line with the model.

This observation is different from previous reports on topological insulators [4,5,7], where the total Hall conductance remained integer valued, even in the case of counter-propagating modes. We note that our devices have a significantly larger separation between the surfaces and that the scattering between counter-propagating modes is therefore reduced. Possible scenarios for the nature of the interaction between the edge modes involve either impurities or a (small) side surface conduction [18]. We model the coupling between counter-propagating modes with an effective mode transmission probability, τ. Then, the probability of reflecting into the mirrored, counter-propagating channel (both opposite charge *and* propagation direction) is $1 - \tau$. When $\tau = 1$, the counter-propagating channels are only coupled through the equilibration of the chemical potential of the edge modes inside the voltage probe electrodes. However, when $\tau = 0$, the counter-propagating channels are fully coupled, and the Hall conductance is found to be integer valued (see Supplemental Material [11] for details). This is most likely the explanation of the integer quantum Hall effect seen in thinner samples. The nonmonotonic change in Hall conductance observed in our case is consistent with a large value of τ [for comparison, also the expected values for $\tau = 0.8$ are shown in Fig. 3(e), which resemble the experimentally observed relative step heights well], as expected for thicker flakes.

Interestingly, the longitudinal resistance, R_{xx}, also behaves differently for parallel propagation and counter-propagating edge modes. For parallel propagation [areas without hatching in Fig. 3(f)], R_{xx} would tend to zero if the edge modes were to become increasingly ideal at higher magnetic field. However, if the two topological surfaces have counter-propagating edge states [hatched regions in Fig. 3(h)], R_{xx} becomes large. We calculated R_{xx} using the Landauer-Büttiker formula (see Supplemental Material [11]). For $\nu_t = \pm 1/2$ and $\nu_b = \mp 1/2$, we find $\rho_{xx} = \frac{h}{\tau e^2}$. If the channels are very transparent ($\tau \approx 1$), R_{xx} should be approximately G_0^{-1}, which can be understood from the equilibration of the chemical potential in the voltage probe electrodes. This situation is also applicable to observations in the HgTe/CdTe quantum spin Hall state, where $\tau = 1$ because of the opposite spin of the modes [10], albeit with a factor of two difference because of the different

Berry phase. If $\tau \ll 1$, the two counter-propagating channels are strongly coupled, since the backscattering rate is high, so R_{xx} is expected to be large. The gate map of R_{xx} at 15 T is shown in Fig. 3(f). The filling factors for both surfaces are indicated using the notation (ν_t, ν_b). It can be seen that both $R_{xx}(\frac{1}{2}, -\frac{1}{2}) = 22.5$ kΩ and $R_{xx}(-\frac{1}{2}, \frac{1}{2}) = 20.5$ kΩ are close to G_0^{-1}, again indicative of τ being close to 1. For the thinner sample of Xu *et al.* [4], based on their measured value for R_{xx}, we estimate $\tau = 0.1$, which is indeed an order of magnitude smaller, indicating more proximate and thus more strongly coupled edge channels, fully consistent with their observation of an integer quantum Hall effect.

IV. CONCLUSION

In conclusion, the Fermi level has been controlled independently for the upper and lower surface states of a 3D topological insulator using a dual-gating configuration. The developing quantum Hall states are observed at a magnetic field of 15 T. Applying the Landauer-Büttiker formalism, we simulate the system for both a parallel and counter-propagation edge state configuration and we experimentally confirm a nonmonotonic change in the Hall conductance for counter-propagating states when compared to the integer quantum Hall effect. Our data suggest that it is the interaction between counter-propagating modes that results in the noninteger quantum Hall effect. The interaction can be understood from the equilibration of the chemical potential in the electrodes and the scattering between the edge modes of the top and bottom surfaces. Future experiments with higher mobility samples or at higher magnetic fields will likely result in fully developed quantum Hall edge states, by which the theory can be compared to the data more directly.

Compared to the well studied electron-hole quantum Hall bilayers in semiconducting 2D heterostructures (e.g., see [19–21]), the topological surface states hold up the intriguing prospect of showing fractional exchange statistics, when combined with superconductivity, due to the helical nature of the edge modes. Counter-propagating and spin-resolved edge modes have also been realized in quantum spin Hall insulators [10] and twisted bilayer graphene [22,23], but scattering between counter-propagating edge modes, as reported here, is only possible for 3D topological insulators, providing an additional control parameter in quantum Hall experiments and applications. The combination of edge mode interaction and potential equilibration in the electrodes might also be a suitable platform to investigate models for scattering in the fractional quantum Hall effect [24] and independent tuning of quantum Hall edge states by the magnetic proximity effect [25–27].

[1] K. v. Klitzing, G. Dorda, and M. Pepper, Phys. Rev. Lett. **45**, 494 (1980).

[2] K. S. Novoselov, Z. Jiang, Y. Zhang, S. V. Morozov, H. L. Stormer, U. Zeitler, J. C. Maan, G. S. Boebinger, P. Kim, and A. K. Geim, Science **315**, 1379 (2007).

[3] M. Z. Hasan and C. L. Kane, Rev. Mod. Phys. **82**, 3045 (2010).

[4] Y. Xu, I. Miotkowski, C. Liu, J. Tian, H. Nam, N. Alidoust, J. Hu, C.-K. Shih, M. Z. Hasan, and Y. P. Chen, Nat. Phys. **10**, 956 (2014).

[5] Y. Xu, I. Miotkowski, and Y. P. Chen, Nat. Commun. **7**, 11434 (2016).

[6] R. Yoshimi, A. Tsukazaki, Y. Kozuka, J. Falson, K. S. Takahashi, J. G. Checkelsky, N. Nagaosa, M. Kawasaki, and Y. Tokura, Nat. Commun. **6**, 6627 (2015).

[7] C. Brüne, C. X. Liu, E. G. Novik, E. M. Hankiewicz, H. Buhmann, Y. L. Chen, X. L. Qi, Z. X. Shen, S. C. Zhang, and L. W. Molenkamp, Phys. Rev. Lett. **106**, 126803 (2011).

[8] C.-Z. Chang *et al.*, Science **340**, 167 (2013).

[9] C.-Z. Chang, W. Zhao, D. Y. Kim, H. Zhang, B. A. Assaf, D. Heiman, S.-C. Zhang, C. Liu, M. H. W. Chan, and J. S. Moodera, Nat. Mater. **14**, 473 (2015).

[10] M. König, S. Wiedmann, C. Brüne, A. Roth, H. Buhmann, L. W. Molenkamp, X.-L. Qi, and S.-C. Zhang, Science **318**, 766 (2007).

[11] See Supplemental Material at http://link.aps.org/supplemental/10.1103/PhysRevB.96.195427 for further explanation on the experimental results and on the methods of analysis.

[12] M. Büttiker, Phys. Rev. B **38**, 9375 (1988).

[13] M. Neupane, S.-Y. Xu, L. A. Wray, A. Petersen, R. Shankar, N. Alidoust, C. Liu, A. Fedorov, H. Ji, J. M. Allred, Y. S. Hor, T.-R. Chang, H.-T. Jeng, H. Lin, A. Bansil, R. J. Cava, and M. Z. Hasan, Phys. Rev. B **85**, 235406 (2012).

[14] T. Arakane, T. Sato, S. Souma, K. Kosaka, K. Nakayama, M. Komatsu, T. Takahashi, Z. Ren, K. Segawa, and Y. Ando, Nat. Commun. **3**, 636 (2012).

[15] V. Fatemi, B. Hunt, H. Steinberg, S. L. Eltinge, F. Mahmood, N. P. Butch, K. Watanabe, T. Taniguchi, N. Gedik, R. C. Ashoori, and P. Jarillo-Herrero, Phys. Rev. Lett. **113**, 206801 (2014).

[16] J. Martin, N. Akerman, G. Ulbricht, T. Lohmann, J. H. Smet, K. von Klitzing, and A. Yacoby, Nat. Phys. **4**, 144 (2007).

[17] N. Borgwardt *et al.*, Phys. Rev. B **93**, 245149 (2016).

[18] Y.-Y. Zhang, X.-R. Wang, and X. C. Xie, J. Phys.: Condens. Matter **24**, 015004 (2012).

[19] E. E. Mendez, L. Esaki, and L. L. Chang, Phys. Rev. Lett. **55**, 2216 (1985).

[20] K. Suzuki, S. Miyashita, and Y. Hirayama, Phys. Rev. B **67**, 195319 (2003).

[21] J. P. Eisenstein and A. H. MacDonald, Nature (London) **432**, 691 (2004).

[22] J. D. Sanchez-Yamagishi, T. Taychatanapat, K. Watanabe, T. Taniguchi, A. Yacoby, and P. Jarillo-Herrero, Phys. Rev. Lett. **108**, 076601 (2012).

[23] J. D. Sanchez-Yamagishi, J. Y. Luo, A. F. Young, B. Hunt, K. Watanabe, T. Taniguchi, R. C. Ashoori, and P. Jarillo-Herrero, Nat. Nanotechnol. **12**, 118 (2017).

[24] C. L. Kane and M. P. A. Fisher, Phys. Rev. B **51**, 13449 (1995).

[25] M. Li *et al.*, Phys. Rev. Lett. **115**, 087201 (2015).

[26] Z. Jiang, C.-Z. Chang, C. Tang, P. Wei, J. S. Moodera, and J. Shi, Nano Lett. **15**, 5835 (2015).

[27] F. Katmis *et al.*, Nature (London) **533**, 513 (2016).